Heterogeneities Affect Solid-State Battery Cathode Dynamics

Kaustubh G. Naik, Bairav S. Vishnugopi, and Partha P. Mukherjee[*]

School of Mechanical Engineering, Purdue University, West Lafayette, IN 47907, USA

[*]*Correspondence*: pmukherjee@purdue.edu

Abstract

Solid-state batteries hold the promise to improve energy and power densities compared to conventional lithium-ion batteries. Among myriad interface and mechanistic challenges plaguing the solid-state batteries, the porous cathode architecture owing to the underlying microstructural heterogeneity poses a critical bottleneck. The spatial variability of solid-solid point contacts and ionic/electronic percolation pathways govern the underlying reaction-transport dichotomy, and ultimately affect the spatio-temporal dynamics. In this work, we postulate the inherent role of mesoscale interactions and delineate how heterogeneities profoundly affect the spatio-temporal evolution of thermo-electrochemical dynamics subject to physical and operational extremes. This study critically examines the importance of solid-solid point contacts manifesting as singularities in thermo-electrochemical hotspot formation, intercalation cascade, and reaction current localization and establishes these as mechanistic pain points for consideration in the future development of improved solid-state battery cathode architectures.

1. Introduction

As conventional lithium-ion batteries approach their theoretical energy density limits, there is a critical need for the development of high energy-density batteries that can meet our society's rapidly growing energy storage demands[1-3]. Among various potential alternatives to the lithium-ion chemistry, the utilization of a lithium metal anode owing to its low electrochemical potential (-3.04 V vs. standard hydrogen electrode), high theoretical capacity (3860 mAh g^{-1}) and low density (0.534 g cm^{-3}) has gained tremendous attention[4-7]. In this regard, the development of solid-state batteries (SSBs) that pair an inorganic solid electrolyte (SE) with the lithium metal anode promise to simultaneously improve the energy density, power density and safety of lithium-ion batteries[8-11]. Various theoretical attributes including the high cationic transference number, mechanical rigidity and non-flammability of SEs have been probed toward assessing limitations such as concentration gradients, morphological stability of the metal anode and thermal instability that are encountered in liquid electrolyte systems[8, 9]. While mechanistic attributes related to interface evolution, chemo-mechanics and transport still need to be addressed in SSBs, recent improvements in the ionic conductivity of SEs[12-16] (e.g., sulfide-based electrolytes) and the stability of the lithium-SE interface[17] (e.g., through interlayers) have shown encouraging rate performance and cycle life.

As the lithium metal anode in SSBs continues to be interrogated to decipher various failure mechanisms such as filament penetration, void growth and interphase formation,[18-26] a comprehensive understanding of the role of transport-reaction interplay, solid-solid interfaces and the underlying heterogeneity in the composite cathode still needs to be attained. The electrochemical performance and internal resistance evolution in SSBs is a strong function of the composition and spatial arrangement of the constituent phases in cathode microstructure, which

determine the distribution of solid-solid contact and ionic/electronic percolation pathways[27-30]. While secondary phases such as carbon additives and binder can improve electronic percolation and mechanical stability of the electrode respectively[31, 32], they result in additional complexities such as blockage of ionic transport and degradation mechanisms at the binder-SE interfaces[28, 33-35]. In addition, secondary phases reduce the active interfacial area between the active material (AM) and SE[35]. Thus, the presence of secondary phases increases the resistance associated with reaction and transport in the composite cathode. Though this influence of secondary phases is also similar in the case of liquid electrolyte cells, the scenario is more severe in solid-state cathodes due to the already limited interfacial contact and percolation pathways. Specifically, the presence of solid-solid point contacts and voids due to the limited wettability of the SEs on the AM surface results in exacerbated overpotentials and highly tortuous transport pathways[36]. With SEs being more mechanically resistant to deformations, large volume fluctuations of the AM have shown to result in loss of electrochemically active area that impose an additional kinetic limitation[35, 37-39]. Though single-ion conductors are expected to mitigate concentration gradients and spatial variability in reactions, due to enhanced ionic tortuosity and the resulting electric potential drop, significant localization of reaction current near the cathode-separator interface has been observed [40-43]. As shown in recent studies, such limitations exacerbate at higher C-rates and higher AM loading, resulting in accelerated capacity fade[44, 45].

To improve the interfacial contact between the AM and SE particles, a wide range of strategies including electrolyte-coated AM particles[46] and liquid-phase synthesized electrolytes[47] have been explored. The effect of size and morphology of the AM and SE particles on active area, transport and the resulting electrode performance has also been analyzed[48, 49]. While Minnmann *et al*.[50] suggested the use of diluent-free cathodes to achieve enhanced performance

for higher AM loadings, Li *et al*.[51] proposed superior mixed ionic/electronic conductor as a substitute for SE and carbon additives to maximize energy density in SSBs. To improve ionic conduction in composite cathodes, the use of fiber-shaped carbon additives over spherical carbon to minimize the carbon content in cathode composite has been recently studied[52]. Overall, though various strategies to improve interfacial contact and percolation pathways have been adopted, the design of solid-state cathodes is fundamentally challenged by the mechanistic tradeoffs (e.g., reaction kinetics vs. transport limitations) that arise when one specific attribute (e.g., secondary phase morphology, AM loading) is regulated.

Previous studies have highlighted various factors such as distribution in particle sizes and shapes, and electrode processing that result in microstructural heterogeneities in the lithium-ion battery electrodes[53-55]. Thus, a fundamental understanding of the coupled role of electrode microstructural stochasticity and the spatio-temporal electrochemical-transport dynamics on the active material utilization and thermal signatures in the solid-state cathode is still required. Importantly, the mechanistic role of heterogeneities arising due to the spatial variability in the electrode microstructural properties (e.g., solid-solid point contacts, tortuosity) on aspects such as the local distribution of reaction current, development of thermo-electrochemical hotspots and the resulting electrochemical performance needs to be investigated. While recent studies have highlighted the important role of electrode heterogeneities in LIBs during operational extremes (e.g., fast charging, low temperature operation)[56, 57], solid-state cathodes pose intrinsic reaction and transport limitations due to solid-solid point contacts and restricted percolation pathways that can lead to current focusing and higher electric potential gradients. We hypothesize that depending on the electrode thickness, current rate and operating temperature, these distinct microstructural features (e.g., AM loading, point contacts) coupled with the heterogeneous nature of their

distribution can mechanistically affect the electrochemical and thermal response of the solid-state cathode. In this work, we develop a hierarchical mesoscale model that quantifies the distribution of effective properties (e.g., active area, tortuosity) in the electrode microstructure and systematically connects it to the electrochemical performance of the SSB. We study how the microstructural heterogeneity in the solid-state cathode intricately governs the spatio-temporal evolution of mechanisms including ion percolation, lithium intercalation and internal heat generation across a wide range of electrode design parameters and operating conditions. Governed by the ion transport limitation and presence of heterogeneities in the cathode, we identify distinct patterns of spatial progression in reaction current focusing, reaction and ohmic heat signatures, and active material utilization. Limitations pertaining to the low temperature operation of SSBs, and the role of heterogeneities in the thermo-electrochemical interaction including the evolution of hotspots have been analyzed. This work provides fundamental insights into the microstructure-coupled mechanistic interactions in the solid-state cathode and highlights the underpinning implications of electrode heterogeneities on the reaction-transport interplay and the resulting electrochemical performance.

2. Methodology

To mechanistically probe the implications of heterogeneities in the composite solid-state cathode, we develop a hierarchical modeling framework that captures the spatial variation in effective electrode properties (e.g., tortuosity, active area) based on the local electrode microstructure. This information regarding the spatial distribution of electrode properties is coupled with a 3D electrochemical performance model to understand the spatio-temporal dynamics of reaction current distribution, active material utilization and intrinsic heat generation. The hierarchical

modeling approach allows us to delineate the role of solid-solid point contacts and transport pathways on these underlying mechanistic interactions. A solid-state cathode with an average composition of 60 wt. % $LiNi_{0.6}Mn_{0.2}Co_{0.2}O_2$ (NMC622) AM, 34 wt. % β-Li_3PS_4 SE, and 6 wt. % PVDF/C carbon-binder domain (CBD), constructed using GeoDict[58, 59] is used as a representative baseline system for this study. It is noted that while the average electrode composition is denoted here, the electrode microstructure includes stochasticity and heterogeneity in the composition of its constituent phases at different sections of the electrode. The mathematical relation to describe the underlying electrode heterogeneity is discussed in the subsequent section. The average volume fraction of voids in the composite cathode is kept at 5% of the total electrode volume. The constructed electrode microstructure is then divided into 9×9 Representative Volume Elements (RVEs) in the in-plane direction (see Figure S1 of the Supporting Information) and the effective electrode properties of all RVEs are estimated using direct numerical simulation (DNS) based on their individual microstructural attributes. The mathematical formulation for effective electrode property estimation is described in the Section S2 of the Supporting Information. For the electrochemical performance simulations, the cathode is further divided into 7 equal segments along the thickness direction. Thus, the total cathode domain is made of $9 \times 9 \times 7$ RVEs. This treatment allows us to not only incorporate the effect of heterogeneities but also comprehensively investigate various spatio-temporal trends along the in-plane and thickness directions of the composite cathode. Since in-plane dimensions of the electrodes are much larger than the electrode thickness, the electrode property variations are more prominent along the in-plane direction when compared to the thickness direction[57, 60]. Thus, the effect of microstructural variability on the effective electrode properties (i.e., ionic tortuosity, active area and effective electronic conductivity) is considered in the in-plane direction in this work. However,

we note that variations in current distribution and active material utilization based on the reaction-transport limitations will still occur along the thickness-direction of the electrode. The 3D electrochemical performance model which considers the spatial variability in the electrode properties is provided in Section S3 of the Supporting Information where the details of the governing equations describing the microstructure-coupled mechanisms including ion transport, electron transport, electrochemical reaction at the AM-SE interface, and solid-state diffusion of lithium in the AM are delineated. Temperature dependency of kinetic and transport properties such as reaction rate constant[61], ionic conductivity[62] and solid-state diffusivity[61] has been incorporated in the model and the corresponding details are provided in Section S4 of the Supporting Information. A quantitative comparison of the electrochemical performance signature obtained using the proposed modeling framework and a recent experimental report[63] has been provided in Section S5 of the Supporting Information, showing a very good agreement.

3. Results and discussions

3.1. Microstructural Heterogeneity and Electrode Properties

For a cathode microstructure (schematic illustration shown in Figure 1(a)) with the following average composition – 60 wt. % AM, 34 wt. % SE, 6 wt. % CBD, Figure 1(a) shows how the composition varies along the in-plane direction, which is illustrated based on the heterogeneity descriptor, d. This descriptor physically represents the local AM content within the cathode microstructure and is mathematically given as follows:

$$d = \frac{\varepsilon_{AM}}{\overline{\varepsilon}_{AM}} - 1 \tag{1}$$

Rearranging the above equation gives:

$$\varepsilon_{AM} = \overline{\varepsilon}_{AM}(d+1) \tag{2}$$

Here, ε_{AM} corresponds to the local AM volume fraction, whereas $\overline{\varepsilon}_{AM}$ is the average AM volume fraction present in the composite cathode. Negative/positive values of d signify that the local AM fraction, ε_{AM}, is lower/higher than the average AM fraction, $\overline{\varepsilon}_{AM}$. In Figure 1(a), as d ranges from -0.5 to 0.5, ε_{AM} varies stochastically from $0.5\,\overline{\varepsilon}_{AM}$ to $1.5\,\overline{\varepsilon}_{AM}$ over the electrode cross-section. Figure 1(b-d) presents the effective electrode property maps, namely, tortuosity for ionic transport, electrochemically active area, and electronic conductivity respectively for the heterogeneous cathode microstructure considered in Figure 1(a). Locations with a lower AM content result in a reduction in tortuosity due to efficient ionic percolation pathways through SE phase (see Figure 1(b)). For instance, the locations with $d = -0.4$ have ionic tortuosity of around 1.2, whereas the locations with $d = 0.5$ have ionic tortuosity of around 4.5 owing to the highly tortuous ionic pathways. Similarly, in Figure 1(d), due to the higher intrinsic electronic conductivity of the CBD phase and better percolation networks, the higher AM-CBD content results in enhanced effective electronic conductivity. As illustrated in Figure 1(c), the spatial variation in active area shows a distinct trend when compared to the tortuosity (Figure 1(b)) and electronic conductivity (Figure 1(d)). Driven by the heterogeneous distribution of the CBD phase, this trend will induce an intrinsic asymmetry in the spatio-temporal evolution of reaction (driven by the point contact distribution) and transport resistances (driven by the SE phase connectivity). The regions with a higher AM fraction ($d \approx 0.5$) result in limited AM-SE contact ($\sim 1.3 \times 10^4$ m^2/m^3) due to insufficient SE content (Figure 1(c)). In addition, the presence of CBD phase results in the blockage of solid-solid contact between the AM and SE particles, leading to further reduction in active area as shown in Figure 1(c). Overall, the heterogeneity in the electrode microstructure

results in spatially varying effective electrode properties that can lead to mechanistic implications including intercalation cascade, non-uniform reactions, and thermal hot spots during electrochemical operation. These implications have been discussed in detail in the following sections.

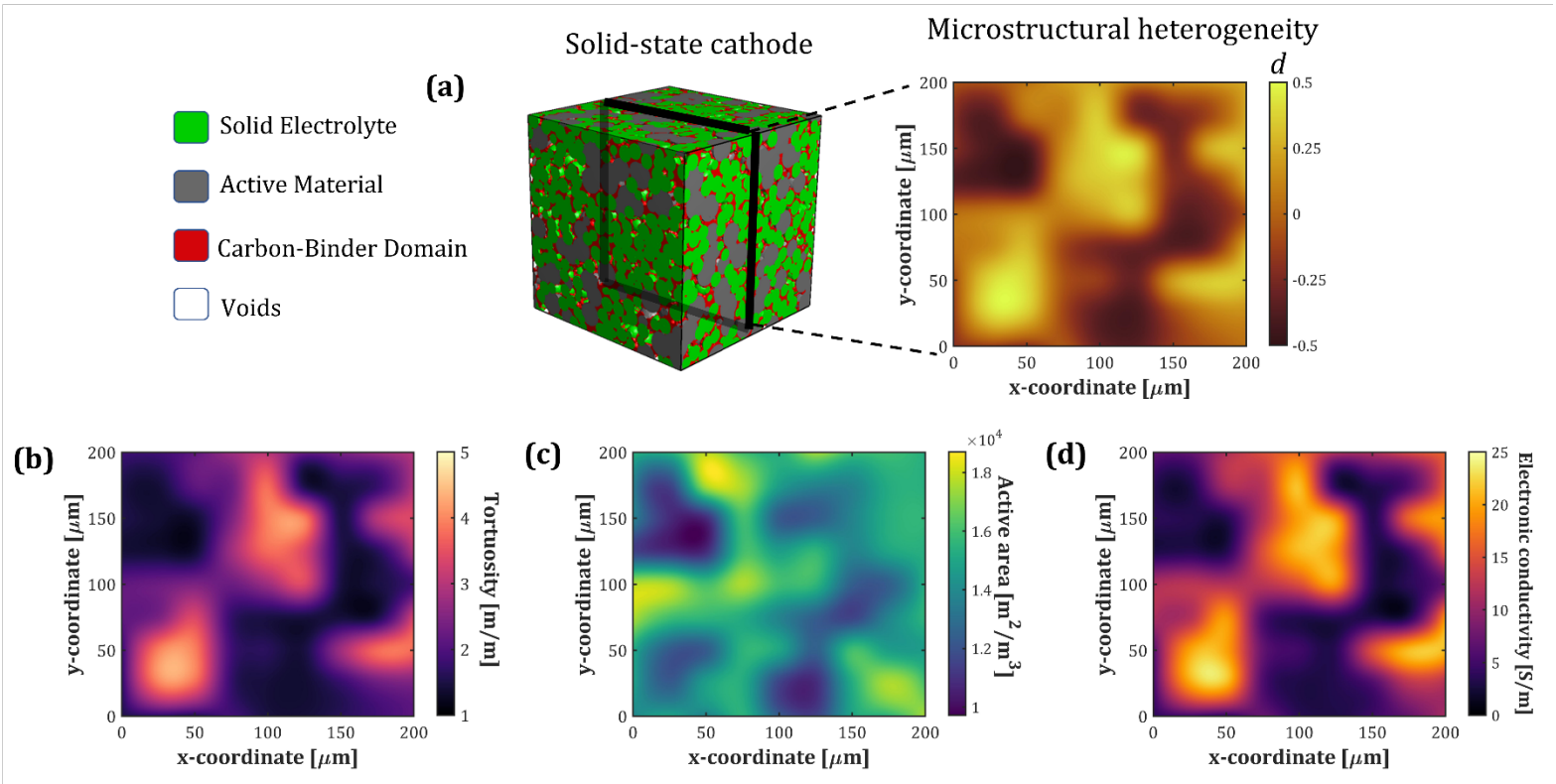

Figure 1. (a) Schematic illustration of a solid-state cathode along with the heterogeneity map for the cathode composition, which is illustrated based on the heterogeneity descriptor, $d = \frac{\varepsilon_{AM}}{\bar{\varepsilon}_{AM}} - 1$. Spatial variation in the effective electrode properties: (b) tortuosity for ionic transport, (c) electrochemically active area, and (d) electronic conductivity, described for the electrode heterogeneity map in (a).

3.2. Mechanistic Role of Heterogeneities in Reaction-Transport Interactions and Electrochemical Performance

For the heterogenous microstructure presented in Figure 1, the electrochemical performance (composite cathode mass specific discharge capacity) and spatio-temporal patterns of lithiation are

analyzed for an electrode thickness of 70μm and a discharge rate of 1C. Figure 2 presents the lithiation state (θ) distribution of the AM particles near the cathode-separator interface at four different time instances (i.e., $t_1^* = 1$ min, $t_2^* = 20$ min, $t_3^* = 45$ min and $t_4^* = 57$ min) during the discharge process. Along with the cell voltage, the difference in particle-level state-of-charge between the most and least utilized AM site ($\Delta\theta$) at the electrode cross-section under consideration, illustrative of the maximum heterogeneity in the lithiation response is presented in Figure 2(a). At the beginning of discharge (at t_1^*), the lithiation state of all the AM sites is nearly constant, showing negligible spatial variation (Figure 2(b)). As discharge progresses, at t_2^*, sections of the electrode with lower AM fractions exhibit preferential intercalation (Figure 2(c)). This is due to the lower transport resistance of these electrode sections (Figure 1(b)) that results in efficient ionic percolation and easier accessibility of these sites for electrochemical reaction. In addition, lesser availability of AM particles in these regions results in rapid lithiation. This preferential lithiation mechanism results in a build-up of lithiation heterogeneity in the electrode, reaching a maximum at t_3^*, as shown in Figure 2(d). Following this, the tendency of the preferentially lithiated AM particles to get further lithiated reduces. This reduction in the lithiation propensity for highly lithiated AM particles is due to the decrease in exchange current density. At a high state-of-charge (θ), the exchange current density of the AM particles rapidly decreases with further lithiation, resulting in a sharp overpotential rise. Thus, within a short time span, the ionic current diverts towards the less lithiated AM particles, resulting in a reduction in the lithiation heterogeneity during later stages of the discharge process. This lithiation heterogeneity map is illustrated at t_4^* in Figure 2(e). As discharge progresses, $\Delta\theta$ increases and reaches maximum at t_3^*, after which it decreases significantly to result in reduced spatial variability. Overall, driven by the spatial distribution in electrode composition and the resulting reaction-transport interaction, we observe

a non-monotonically varying trend in the lithiation heterogeneity. As discussed later, the underlying asymmetry in the reaction-transport interaction and the spatio-temporal variation in the lithiation dynamics that have been described in Figure 2 will have a critical implication for thicker electrodes and higher discharge rates.

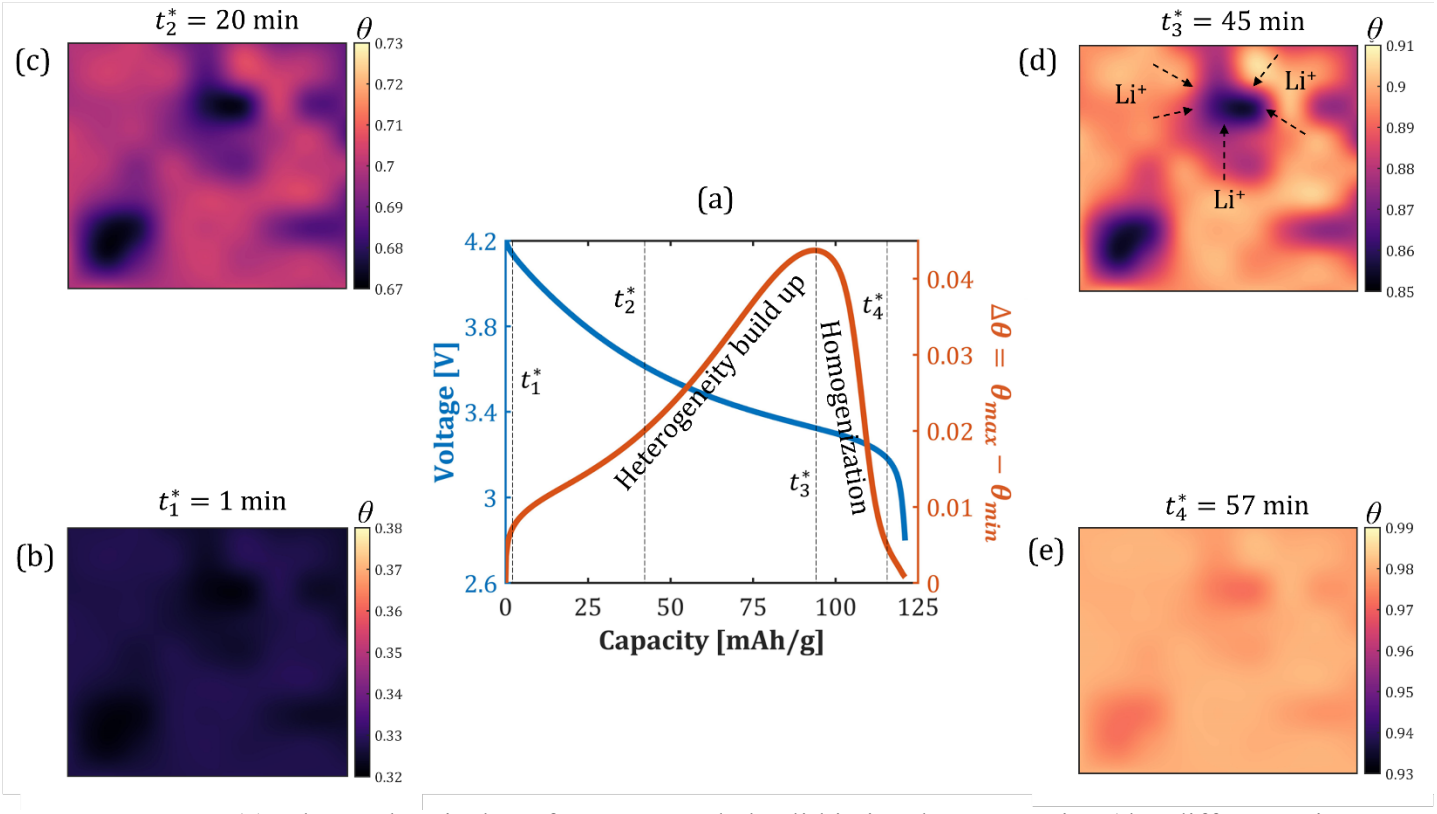

Figure 2. (a) Electrochemical performance and the lithiation heterogeneity (the difference in particle-level state-of-charge of the most and the least utilized AM sites ($\Delta\theta$)) evolution for electrode thickness of 70μm and discharge rate of 1C. Lithiation heterogeneity maps at 4 different time instances, namely, (b) $t_1^* = 1$ min, (c) $t_2^* = 20$ min, (d) $t_3^* = 45$ min, and (e) $t_4^* = 57$ min during the discharge process. Evolution of the lithiation heterogeneity in (a) suggests preferential lithiation due to microstructural heterogeneity leading to intercalation cascade, followed by rapid intercalation of the unlithiated sites resulting in reduced lithiation heterogeneity at the end of discharge.

Driven by the heterogeneity in the cathode microstructure, the electrochemical performance and lithiation heterogeneity for different C-rates are depicted in Figure 3. As the C-rate is increased, the higher transport resistance and enhanced overpotentials at the solid-solid point contacts pose

limitations on the cell performance (Figure 3(a)). As discussed in the previous section, electrode heterogeneity leads to preferential intercalation followed by a quick diversion of ionic transport toward less intercalated AM sites. The lithiation heterogeneity for the corresponding C-rates represented in Figure 3(a) is quantified at the separator and current collector ends of the cathode (based on $\Delta\theta$), as shown in Figure 3(b). As mentioned in the previous section, $\Delta\theta$ represents the difference in particle-level state-of-charge between the most and least utilized AM site ($\Delta\theta$) at a given electrode cross-section. From the $\Delta\theta$ variation shown in Figure 3(b), it is inferred that the separator side of the electrode exhibits minimal lithiation heterogeneity even with an increase in C-rate at the end of discharge. On the other hand, the lithiation heterogeneity near the current collector at the end of discharge shows a significant increase with C-rate, illustrating the spatio-temporal non-uniformity in active material utilization across the electrode. After reaching the point of maximum lithiation heterogeneity, it is interesting to note that even though ion transport is diverted towards the less utilized AM sites, for the 2C and 3C cases, these AM sites at the current collector side do not get fully utilized (Figure 3(d) and 3(e)). On the other hand, the less utilized AM sites get almost fully lithiated for the 1C case, as shown in Figure 3(c). An increase in C-rate leads to a higher lithiation heterogeneity and a lower overall active material utilization, driving the cell voltage toward the cut-off value (i.e., 2.8V) at lower capacities (illustrated in Figure 3(a) and 3(b)). While the intrinsic ion transport limitation of the solid-state cathode results in localized reactions near the separator (i.e., heterogeneity along the thickness direction), further spatio-temporal variability and limitation in lithiation response is induced by the in-plane heterogeneities in the electrode microstructure. Driven by the spatial variation in ionic transport (i.e., tortuosity), the mechanistic limitation due to the heterogeneity in electrode microstructure exacerbates at higher C-rates.

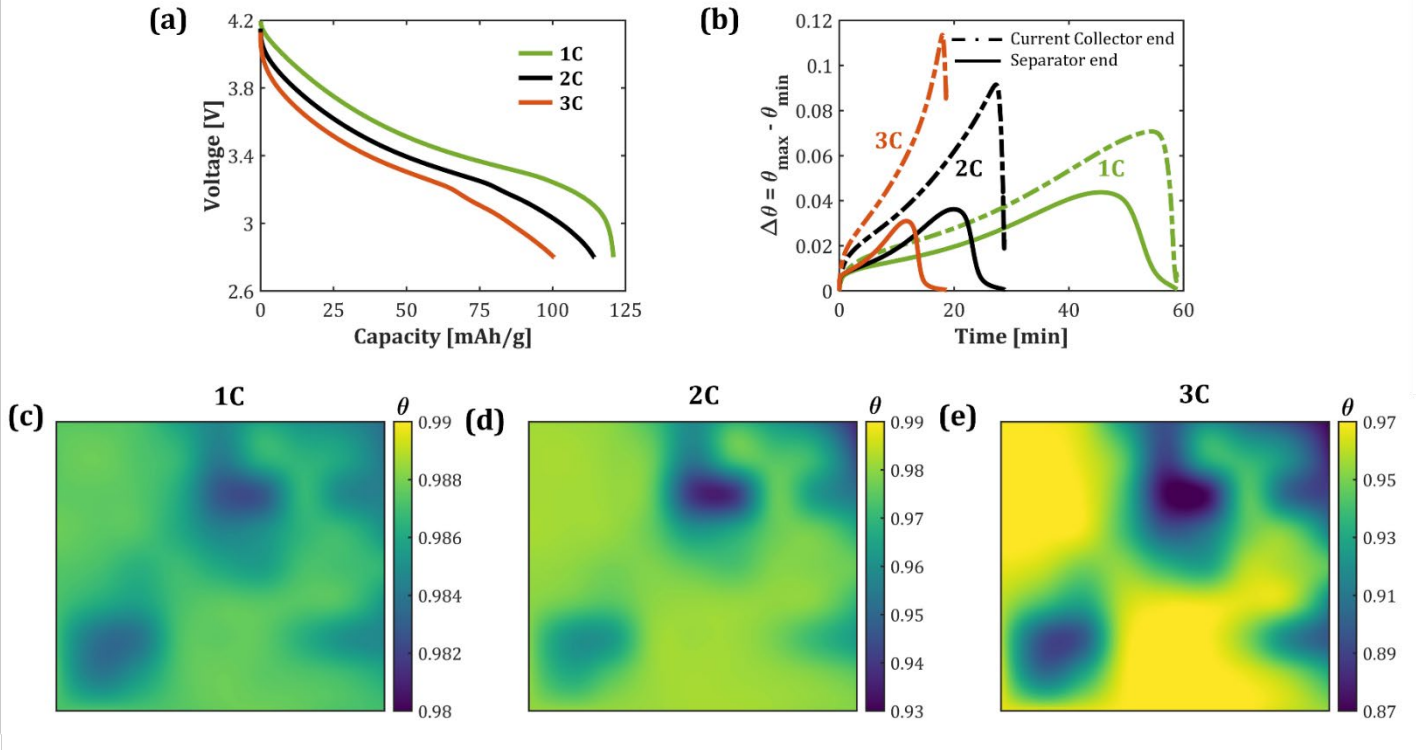

Figure 3. (a) Electrochemical performance of the heterogeneous cathode (70μm thickness) at C-rates of 1C, 2C and 3C. (b) Dynamic evolution of the difference in particle-level state-of-charge of the highest and least utilized AM sites ($\Delta\theta$) at the separator and current collector end of the cathode. Lithiation heterogeneity maps at the current collector end during the end of discharge for (c) 1C, (d) 2C, and (e) 3C.

As discussed in the earlier section, the lithiation heterogeneity becomes more prominent as we go from separator to current collector side of the cathode. To further investigate this phenomenon, we probe the how the intercalation heterogeneity scales with the cathode thickness. Figure 4(a) presents the electrochemical performance for different cathode thicknesses of 35μm, 70μm, and 120μm for a 1C discharge rate. Due to the longer ionic percolation pathways, ionic transport resistance is higher for thicker cathodes that results in a reduced capacity as shown in Figure 4(a). Lithiation heterogeneity at the current collector end is quantified in Figure 4(b) based on the temporal evolution of $\Delta\theta$. Since the lithiation heterogeneity on separator side reduces towards the end of discharge (as seen in Figure 3(b)), our major focus is to the understand the heterogeneity

evolution at the current collector side for different cathode thicknesses, as shown in Figure 4(b). For the 35μm and 70μm cathode thicknesses, the lithiation heterogeneity increases and reaches a maximum, following which it reduces due to diversion of ionic transport towards the less utilized AM sites. Thus, almost complete AM utilization is observed in case of 35μm and 70μm as seen from lithiation maps in Figure 4(c) and Figure 4(d) respectively, with the latter being slightly less utilized. This is also consistent with the final cell capacities that are shown in Figure 4(a). On the other hand, for a cathode thickness of 120μm, the lower cut-off for cell voltage (2.8V) is already reached while there is a build-up in the intercalation heterogeneity (Figure 4(b)). Thus, the diversion in the ionic flux from the more utilized to the less utilized AM sites does not take place before the end of discharge. Driven by the longer ionic transport pathways, even the least resistive AM sites are not fully lithiated near the current collector for a cathode thickness of 120μm (Figure 4(c)). This leads to a large reduction in cell performance as shown in Figure 4(a). The higher ionic transport resistance coupled with the intrinsic electrode heterogeneity results in significantly less active material utilization for thicker cathodes. Thus, for such thicker cathode configurations, improvement in ion percolation pathways is critical toward countering the negative implications of intrinsic heterogeneity on cell performance. Complimentary to the modeling insights delineated in this work, mapping lithiation heterogeneities using advanced experimental techniques[64, 65] can further our understanding on the role of electrode heterogeneities in SSBs.

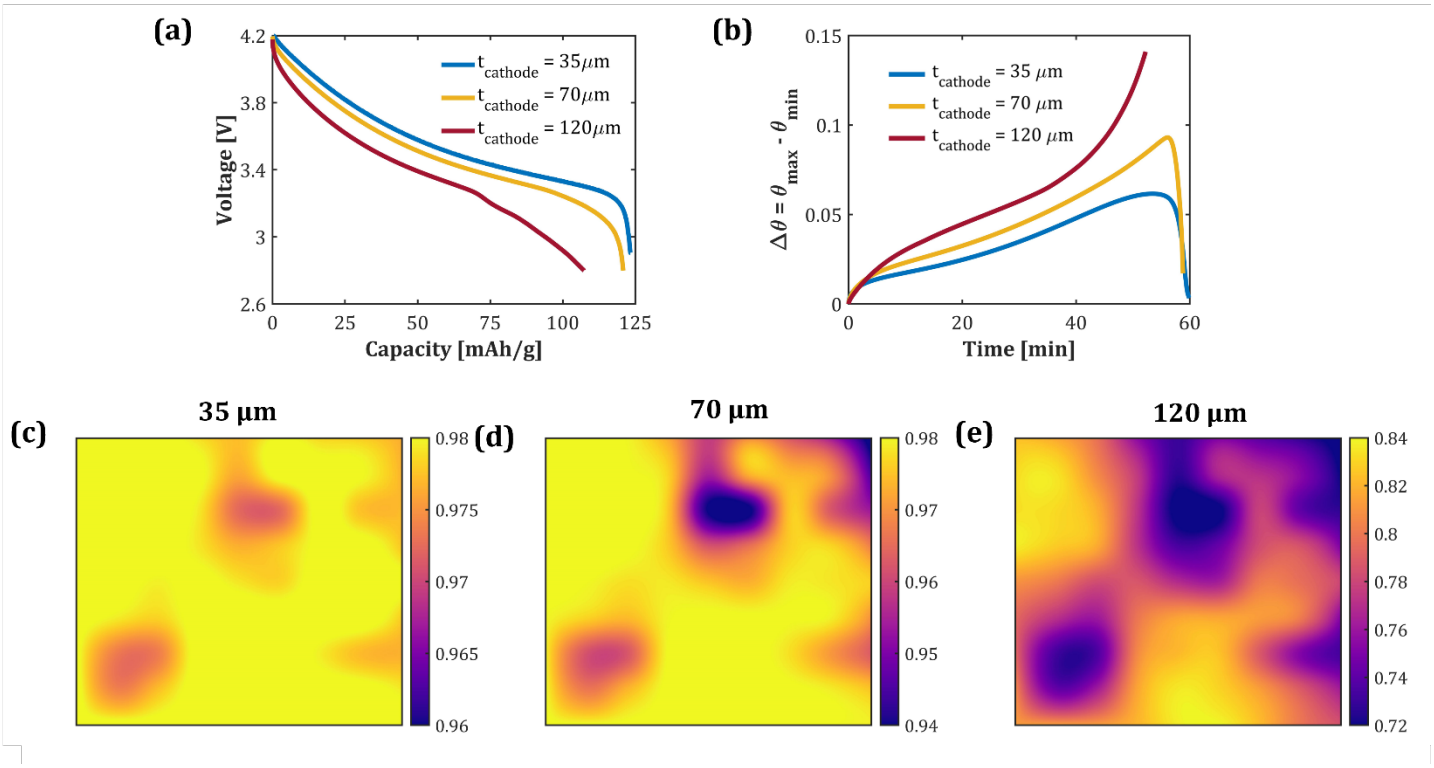

Figure 4. (a) Electrochemical performance of the heterogeneous cathode for thicknesses of 35μm, 70μm, and 120μm at discharge rate of 1C. (b) Dynamic evolution of the difference in particle-level state-of-charge of the most and the least utilized AM sites ($\Delta\theta$) at the current collector end for the cathode thicknesses shown in (a). Lithiation heterogeneity maps at the end of discharge for cathode thicknesses of (c) 35μm, (d) 70μm, and (e) 120μm at the current collector end.

Driven by the ion transport and electrochemical reactions, and the intrinsic heterogeneity in these mechanistic interactions, internal cell temperature plays a pivotal role on the AM utilization and reaction heterogeneity. The temperature-dependent reaction-transport interactions in the cathode and the resulting cell performance is probed here. Figure 5(a) presents the electrochemical performance of the heterogeneous cathode microstructure for operating temperatures between -20ºC and 60ºC. Temperature dependency of the ionic conductivity of β-Li_3PS_4 SE[62, 66, 67], solid-state diffusivity of lithium in NMC622 AM particles[61], and reaction rate constant[61] has been investigated in the literature (see Section S4 of the Supporting Information), illustrating the critical role of temperature on the transport and reaction mechanism. As shown in Figure 5(a),

discharge capacity increases from 30 mAh/g to 75 mAh/g as cell temperature in increased from -20 ^{0}C to 0 ^{0}C and to 115 mAh/g and 122 mAh/g for cell temperatures of 20 ^{0}C and 40 ^{0}C. However, further increment in cell temperature has a negligibly small effect on the delivered capacity as complete AM utilization has already been achieved. At low cell temperatures, ion percolation from the separator to the current collector side is limited due to the substantially lower ionic conductivity that results in a steep drop in the AM utilization at the current collector side. This can be inferred from the lithiation heterogeneity map shown in Figure 5(b). In addition, reduced solid-state diffusivity of lithium in AM at low temperatures leads to higher overpotential and subsequently, lower AM utilization. On the other hand, while there is an improvement in the AM utilization at 20 ^{0}C, lithiation heterogeneity still exists at the end of discharge since ions cannot percolate into the regions with higher AM fraction (Figure 5(c)). Increasing the cell temperature to 40 ^{0}C leads to almost complete and homogeneous AM utilization (Figure 5(d)) due to enhanced ion transport and solid-state diffusion that leads to improved discharge capacity as shown in Figure 5(a). Thus, temperature assisted enhancement in transport can overcome the negative implications of intrinsic heterogeneity by enabling complete utilization of the electrode via ionic current diversion to the unutilized AM sites as discussed in Figure 2. Since the maximum AM utilization is achieved at 40 ^{0}C, further increase in cell temperature has a minor improvement on the delivered capacity indicating that the electrochemical performance is no longer limited by the ionic transport. Thus, for a particular cathode thickness, composition, and discharge rate, a critical window of operating temperature can provide the required ionic percolation through the SE phase to enable complete lithiation of the AM particles. Figure 5(e-g) represent the variation in electrode averaged state-of-charge (θ_{avg}) for cathode thicknesses ranging from 35μm to 120μm and discharge rates from 0.5C to 3C at cell temperatures of 0 ^{0}C, 20 ^{0}C, and 40 ^{0}C respectively. Here, the phase maps are divided

into regimes I and II denoting complete and incomplete utilization of cathode respectively. As the cathode thickness is increased, the ionic transport resistance in the SE phase increases resulting in lower AM utilization near the current collector. Moreover, at higher C-rates, ion transport from one end to another end of the cathode becomes limiting. Hence, an improvement in ion percolation is critical to enable thicker cathodes for high C-rate applications. As shown in Figure 5(e-g), higher cell temperatures promote enhanced ionic percolation resulting in improved cathode utilization and higher discharge capacities over a broader range of cathode thicknesses. However, a mechanistic tradeoff based on the cathode thickness and discharge rate is observed at all cell temperatures. In other words, increasing the cathode thickness reduces the maximum C-rate at which complete utilization can be achieved. For example, for a cathode thickness of 50μm at 40 ^{0}C (Figure 5(g)), complete cathode utilization can be achieved for discharge rates as high as 3C. However, for a thickness of 80μm, complete AM utilization is observed up to a discharge rate of 1.5C. Overall, an increase in internal temperature alleviates the severity of this tradeoff and through homogenization of the intercalation response, enables improved AM utilization and capacities for thicker cathodes.

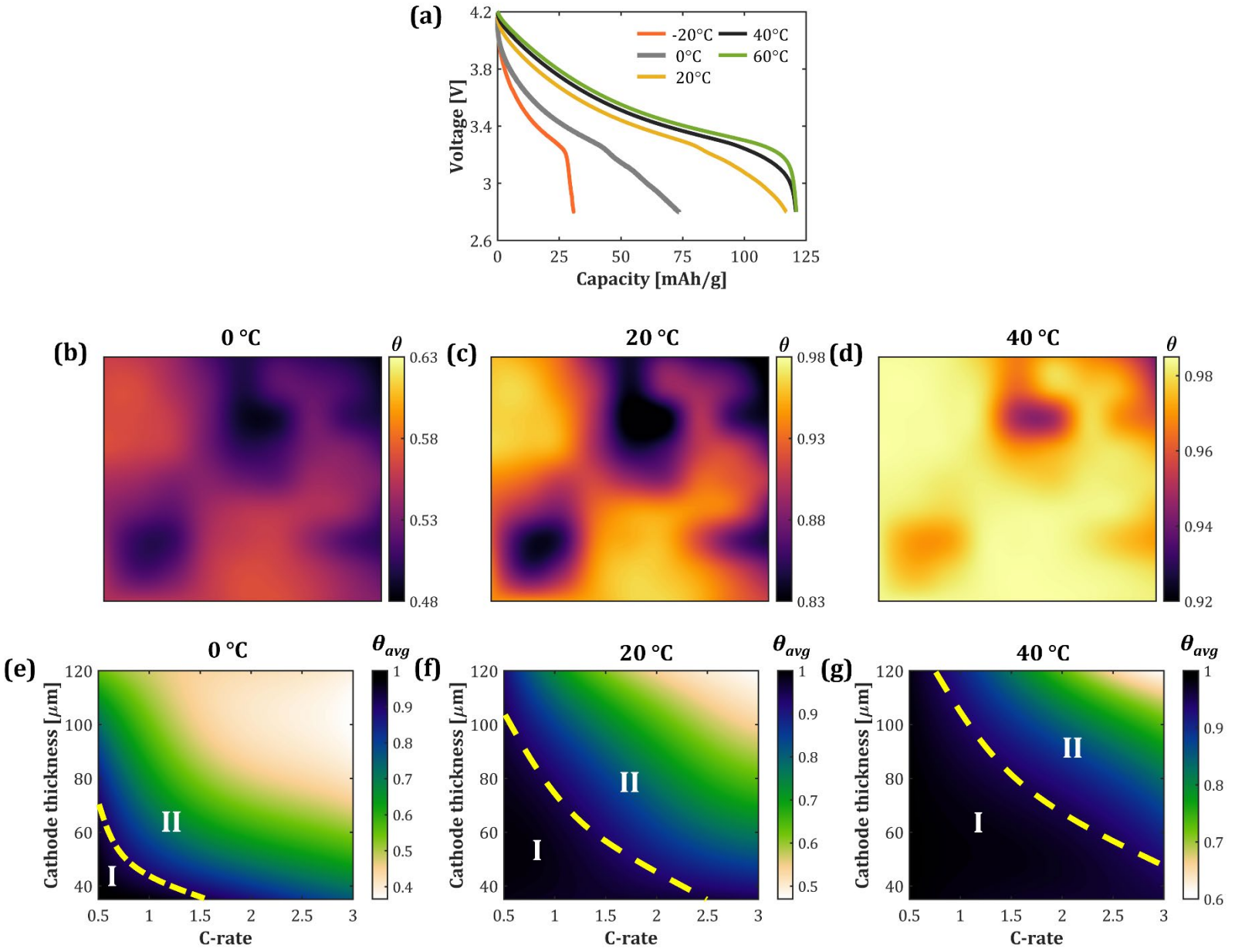

Figure 5. (a) Electrochemical performance of the heterogenous cathode microstructure (70μm thickness) for different cell temperatures at discharge rate of 1C. Lithiation heterogeneity maps at the current collector end during the end of discharge for cell temperatures of (b) 0 ^{0}C, (c) 20 ^{0}C, and (d) 40 ^{0}C. Phase map of electrode averaged state-of-charge (θ_{avg}) at the end of discharge for varying cathode thicknesses and discharge rates at (e) 0 ^{0}C, (f) 20 ^{0}C, and (g) 40 ^{0}C, demarcating complete (regime I) and incomplete (regime II) cathode utilization regimes.

3.3. Spatio-Temporal Evolution of the Intrinsic Heat Generation

Within the solid-state cathode, ion transport through the SE phase that involves an electric potential gradient and reaction current at the solid-solid point contacts between the AM and SE phases are primary sources of intrinsic heat generation. Based on the underlying reaction-transport interactions, the spatio-temporal evolution of intrinsic heat generation within the solid-state cathode and its correlation with the intrinsic electrode heterogeneity is studied here. The resistance to ionic and electronic transport inside SE and AM-CBD phases contribute to the ohmic heat generation inside composite cathode, whereas the overpotential for electrochemical reactions occurring at AM-SE interface is responsible for the reaction heat generation at the solid-solid point contacts. The local ohmic and reaction heat generation rates, $\dot{Q}_{ohmic}$ and $\dot{Q}_{reaction}$, respectively, are mathematically expressed as follows:

$$\dot{Q}_{ohmic} = \kappa_{SE}^{eff} \nabla \phi_{SE} . \nabla \phi_{SE} + \sigma_{elec}^{eff} \nabla \phi_{AM-CBD} . \nabla \phi_{AM-CBD} \quad (3)$$

$$\dot{Q}_{reaction} = j * (\phi_{AM-CBD} - \phi_{SE} - U_{OCP}) \quad (4)$$

Here, κ_{SE}^{eff} and ϕ_{SE} are the effective ionic conductivity and electric potential in SE phase, σ_{elec}^{eff} and ϕ_{AM-CBD} denote the effective electronic conductivity and potential in AM-CBD phase, j is the reaction current density and U_{OCP} is the open circuit potential. Since both the electric potential gradient (based on percolation pathways) and reaction current distribution (based on the solid-solid point contact distribution) are strongly dependent on the electrode microstructure, the underpinning heterogeneities will influence the spatio-temporal evolution of reaction and ohmic heat. It is noted that due to the lack of lithium-ion concentration gradients in the SE phase, its corresponding contribution to the ohmic heat generation is also negligible in the context of single-ion conductors. Figure 6(a) shows the dynamic evolution of the electrode averaged reaction heat

($\bar{\dot{Q}}_{reaction}$) and ohmic heat (ionic ($\bar{\dot{Q}}_{ionic}$) and electronic ($\bar{\dot{Q}}_{elec}$)) generation rates in the heterogeneous cathode at a discharge rate of 1C. Electron transport resistance in the AM-CBD phase is negligible due to high intrinsic electronic conductivity of the CBD phase, resulting in negligible $\bar{\dot{Q}}_{elec}$ as shown in Figure 6(a). Hence, hereafter, ohmic heat due to electron transport will be neglected in our analysis and the term ohmic heat will refer to the heat generated due to ion transport resistance ($\bar{\dot{Q}}_{ionic}$). $\bar{\dot{Q}}_{reaction}$ and $\bar{\dot{Q}}_{ionic}$ remain almost constant around 1×10^5 W/m^3 and 0.25×10^5 W/m^3 until $t = 0.8$h (except a small rise in $\bar{\dot{Q}}_{ionic}$ at the start of discharge), after which both these heat generation rates exhibit a significant increase to 1.4×10^5 W/m^3 and 0.7×10^5 W/m^3 during the end of discharge. This increasing trend in $\bar{\dot{Q}}_{reaction}$ and $\bar{\dot{Q}}_{ionic}$ is governed by the rapid increase in overpotential and electric potential drop in the SE phase respectively. In addition, a higher magnitude of reaction heat when compared to ohmic heat is observed, which is primarily attributed to the presence of solid-solid point contacts that result in reaction current focusing and higher overpotentials. These point contacts are a distinct feature of the solid-state cathode, which is also fundamentally different from a conventional lithium-ion battery electrode where the entire surface of the AM is wet by the liquid electrolyte. The heat generation map, as shown in Figure 6(a), can increase the internal temperature of the SSB cell (see Section S6 of the Supporting Information). In Figure 6(b-d), the reaction heat estimated in each RVE has been mapped to the active reaction sites in the electrode at different stages of discharge. At the beginning of discharge ($t = 10$s), as majority of the reaction is focused near the separator, the reaction heat is also localized near this region as shown in Figure 6(b). Also, we infer that the in-plane variation in reaction heat is determined by the distribution of AM sites (see Figure 1(a)). Sections of the electrode with a higher AM fraction and more solid-solid point contacts generate a larger reaction heat than the sections with a lower AM fraction. At $t = 10$s, as ionic percolation

is restricted near the separator side and incoming lithium ions encounter the unutilized AM sites near the separator, reaction heat is concentrated near the separator-cathode interface. As discharge proceeds and ions transport inside the cathode, the reaction heat concentration also spatially progresses from the separator to the current collector region. At the middle of discharge ($t = 0.5$h), due to the percolation of lithium ions within the cathode and the subsequent electrochemical reactions at the corresponding AM sites, reaction heat generation is observed throughout the cathode domain as seen in Figure 6(c). In addition, as the reactions occur over a larger and distributed interfacial area, the maximum local reaction heat is lowered to 1.6×10^5 W/m^3 (at the middle of discharge) from 3×10^5 W/m^3 at the beginning of discharge. Toward the end of discharge ($t = 0.97$h), as almost all the AM sites are completely lithiated, reaction heat is focused on only a few remaining unutilized AM sites near the current collector as shown in Figure 6(d). Owing to higher tortuosity for ionic transport and more availability of AM for the electrochemical reactions, electrode sections with the highest AM fraction at the current collector end are the last to get fully lithiated. At this instance, the reaction heat generation rate at these locations is as high as 9.5×10^5 W/m^3 (Figure 6(d)), resulting in severe thermal hot spots at the current collector end. Unlike at the start of discharge when all the AM sites are available for lithiation, at the end of discharge, only a few localized AM sites are available for lithiation and thus, heterogeneity plays a critical role on the thermo-electrochemical interactions. Importantly, driven by the intrinsic electrode heterogeneity, towards the end of discharge, thermal hotspots develop at locations with a higher AM fraction near the current collector (Figure 6(d)). The mechanisms at the end of discharge ($t = 0.97$h) is further investigated by plotting the electric potential field in SE phase and the corresponding ionic current vectors at $x = 25\mu$m and $x = 100\mu$m planes as shown in Figures 6(h) and 6(i) respectively. Based on the non-uniform potential profile in SE phase, ionic

flux is diverted towards the unutilized AM sites that results in current focusing at regions with a higher AM content near the current collector. The current constriction observed in Figures 6(h) and 6(i) results in additional resistances within the electrode affecting the electrochemical performance. It is noted that the microstructural heterogeneities govern the electrode-scale current constriction, whereas solid-solid point contacts between AM and SE particles dictate particle-level current constriction. Thus, heterogeneity-induced spatio-temporal evolution of the reaction-transport interactions has a strong influence on the overall battery performance. In this regard, the distribution of the constituent phases (electrode-scale heterogeneity) and solid-solid point contacts between the AM and SE particles (particle-scale heterogeneity) plays a significant role in determining the origin and evolution of thermo-electrochemical hotspots in the cathode.

In Figure 6(e-g), the spatial evolution of ohmic heat generation rates within the SE phase is shown at the start ($t = 10\text{s}$), middle ($t = 0.5\text{h}$) and end ($t = 0.97\text{h}$) of discharge. Ohmic heat generation is localized near the separator side at the beginning of discharge and keeps spreading towards the current collector side as the potential drop builds up along the thickness direction during discharge (See Figure 6(e-g)). It is noted that the ohmic heat generation is always maximum near the separator due to the higher electric potential drop in this region. While the maximum local reaction heat rate in the electrode shows a non-monotonic trend (see Figures 6(b-d)), the magnitude of maximum local ohmic heat generation increases monotonically through the discharge process. Interestingly, in contrast to the spatial variation in the reaction heat generation rates, locations with lower tortuosity (lower AM fraction) experience a higher ohmic heat generation, as illustrated in Figure 6(e-g). SE phase within the composite cathode can be treated as a network with multiple resistances connected in parallel, for such scenario, least resistive pathways (lower tortuosity or

lower AM fraction) would produce maximum ohmic heat which explains the ohmic heat generation trends seen in Figure 6(e-g).

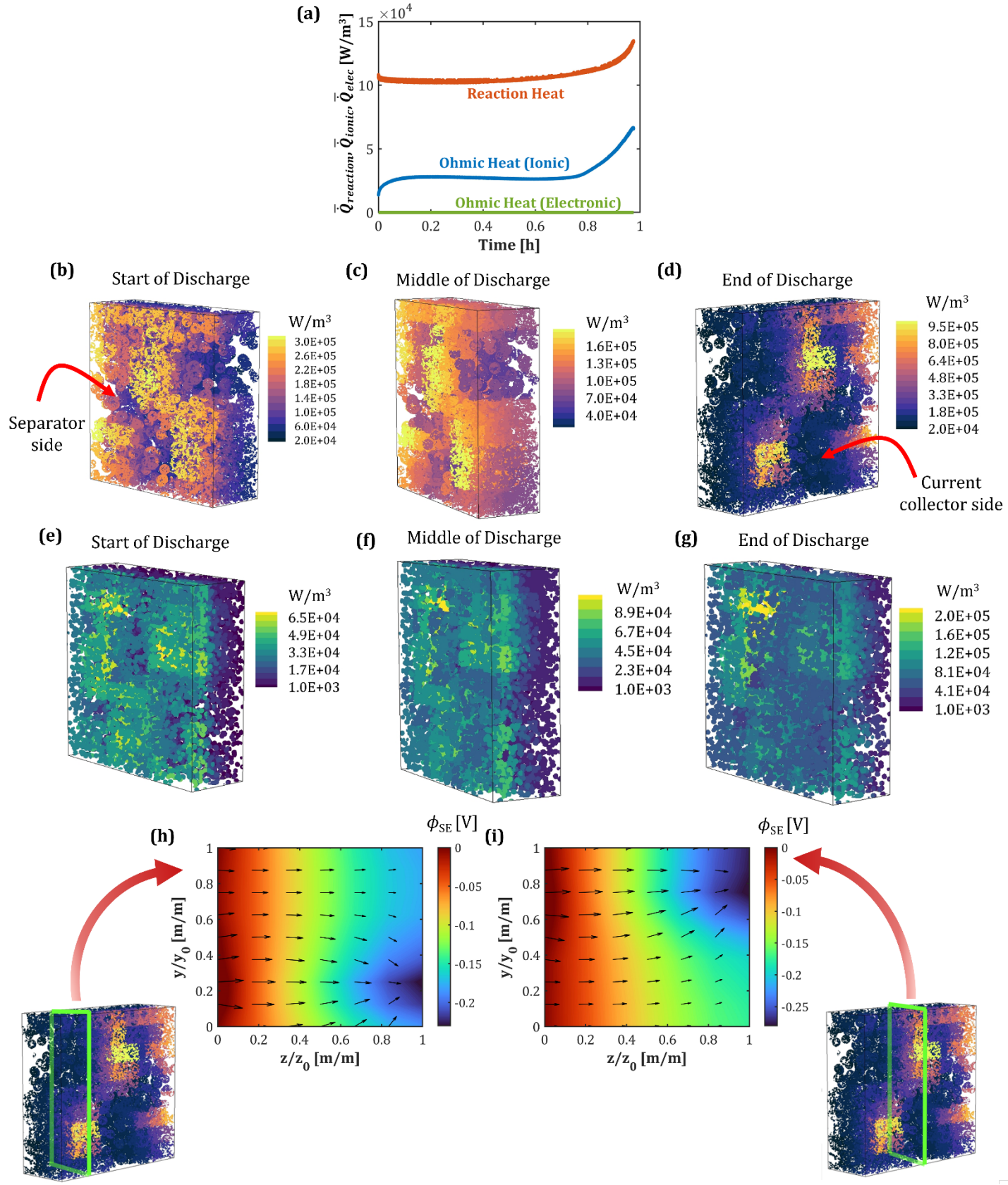
(a)
×10^4
15
10
5
0
$\bar{Q}_{reaction}$, $\bar{Q}_{ionic}$, $\bar{Q}_{elec}$ [W/m³]
Reaction Heat
Ohmic Heat (Ionic)
Ohmic Heat (Electronic)
0
0.2
0.4
0.6
0.8
1
Time [h]
(b)
Start of Discharge
W/m³
3.0E+05
2.6E+05
2.2E+05
1.8E+05
1.4E+05
1.0E+05
6.0E+04
2.0E+04
Separator side
(c)
Middle of Discharge
W/m³
1.6E+05
1.3E+05
1.0E+05
7.0E+04
4.0E+04
(d)
End of Discharge
W/m³
9.5E+05
8.0E+05
6.4E+05
4.8E+05
3.3E+05
1.8E+05
2.0E+04
Current collector side
(e)
Start of Discharge
W/m³
6.5E+04
4.9E+04
3.3E+04
1.7E+04
1.0E+03
(f)
Middle of Discharge
W/m³
8.9E+04
6.7E+04
4.5E+04
2.3E+04
1.0E+03
(g)
End of Discharge
W/m³
2.0E+05
1.6E+05
1.2E+05
8.1E+04
4.1E+04
1.0E+03
(h)
ϕ_{SE} [V]
0
-0.05
-0.1
-0.15
-0.2
y/y0 [m/m]
z/z0 [m/m]
(i)
ϕ_{SE} [V]
0
-0.05
-0.1
-0.15
-0.2
-0.25
y/y0 [m/m]
z/z0 [m/m]

Figure 6. (a) Dynamic evolution of the electrode averaged reaction ($\bar{\dot{Q}}_{reaction}$) and ohmic (ionic ($\bar{\dot{Q}}_{ionic}$) and electronic ($\bar{\dot{Q}}_{elec}$)) heat within the electrode microstructure at 1C. Spatial evolution of the volumetric reaction heat generated at the solid-solid point contacts at (b) start of discharge ($t = 10$s), (c) middle of discharge ($t = 0.5$h), and (d) end of discharge ($t = 0.97$h). Spatial evolution of the volumetric ohmic heat generated in the SE phase at (e) start of discharge ($t = 10$s), (f) middle of discharge ($t = 0.5$h), and (g) end of discharge ($t = 0.97$h). Electric potential field in SE phase and ionic current vectors along (h) $x = 25\mu$m and (i) $x = 100\mu$m planes at the end of discharge ($t = 0.97$h).

Thus, the presence of microstructural heterogeneities induces an asymmetric pattern of reaction and transport heat signatures, with distribution of AM and SE phases, and solid-solid point contacts having a major influence on the spatio-temporal variation of thermal hotspots in the electrode. In addition to the microstructural heterogeneities that dictate the heat generation signatures, thermal conductivities of the constituent cathode phases can alter the local thermal gradients. It is noted that the lithiation heterogeneity coupled with the thermal hotspots can have potential chemo-mechanical implications. In this regard, the role of heterogeneities on the volume change of the cathode, internal stress evolution, and the resultant cell performance will be studied in our future work.

4. Conclusion

In summary, this work presents a comprehensive insight into the role of electrode heterogeneities on the microstructure-coupled reaction-transport interactions and the spatio-temporal electrochemical-thermal response in the solid-state cathode. The spatial variability in electrode attributes such as solid-solid point contacts and percolation pathways results in heterogeneous signatures including non-uniform reaction distribution, intercalation cascade and thermal hotspots. During discharge, we uncover a distinct pattern of electrochemical response where the intercalation heterogeneity exhibits a sharp increase followed by a diversion of ionic current toward unutilized active material sites. However, the effect of electrode heterogeneity manifests

more severely at thicker electrodes and higher C-rates, preventing the complete utilization of the active material and resulting in reduced achievable cell capacity. We quantitatively delineate the mechanistic limitations including reaction heterogeneity, transport, and active material utilization during low temperature operation of the SSB. Based on the intrinsic electrode inhomogeneities and the transport limitation, a spatial progression in reaction current focusing from the cathode-separator interface to the current collector-cathode interface is identified during the discharge process. In addition to limited active material utilization, the thermo-electrochemical interaction driven by such intrinsic heterogeneities results in non-uniform heat generation patterns in the cathode. While an asymmetric spatio-temporal evolution of the reaction and ohmic heat signatures occurs during electrochemical operation, the distribution of solid-solid point contacts has a critical influence on the origin of thermal hotspots in the cathode microstructure. Overall, depending on operating conditions such as temperature and C-rate, and electrode design factors such as thickness and active material loading, heterogeneities in the electrode microstructure manifest with varying severities and mechanistic limitations on the electrochemical performance of SSBs.

Supporting Information

Details of the modeling framework including tables of parameters and verification are included.

Acknowledgement

Financial support in part from the National Science Foundation (award no.: 2041499) and the Alfred P. Sloan Foundation through a Scialog – Advanced Energy Storage award is gratefully acknowledged.

Conflict of Interest

There are no conflicts to declare.

Keywords

solid-state battery, cathode microstructure, electrode heterogeneities, reaction kinetics-transport interaction, solid-solid point contact, electrochemical-thermal interaction, electrochemical performance.

References:

[1] Choi JW, Aurbach D. Promise and reality of post-lithium-ion batteries with high energy densities. Nature Reviews Materials. 2016;1:1-16.
[2] Nitta N, Wu F, Lee JT, Yushin G. Li-ion battery materials: present and future. Materials today. 2015;18:252-64.
[3] Goodenough JB, Kim Y. Challenges for rechargeable Li batteries. Chemistry of materials. 2010;22:587-603.
[4] Lin D, Liu Y, Cui Y. Reviving the lithium metal anode for high-energy batteries. Nature nanotechnology. 2017;12:194-206.
[5] Guo Y, Li H, Zhai T. Reviving lithium-metal anodes for next-generation high-energy batteries. Advanced materials. 2017;29:1700007.
[6] Cheng X-B, Zhang R, Zhao C-Z, Zhang Q. Toward safe lithium metal anode in rechargeable batteries: a review. Chemical reviews. 2017;117:10403-73.
[7] Xu W, Wang J, Ding F, Chen X, Nasybulin E, Zhang Y, et al. Lithium metal anodes for rechargeable batteries. Energy & Environmental Science. 2014;7:513-37.
[8] Hatzell KB, Chen XC, Cobb CL, Dasgupta NP, Dixit MB, Marbella LE, et al. Challenges in lithium metal anodes for solid-state batteries. ACS Energy Letters. 2020;5:922-34.
[9] Krauskopf T, Richter FH, Zeier WG, Janek Jr. Physicochemical concepts of the lithium metal anode in solid-state batteries. Chemical Reviews. 2020;120:7745-94.
[10] Liu J, Bao Z, Cui Y, Dufek EJ, Goodenough JB, Khalifah P, et al. Pathways for practical high-energy long-cycling lithium metal batteries. Nature Energy. 2019;4:180-6.
[11] Vishnugopi BS, Kazyak E, Lewis JA, Nanda J, McDowell MT, Dasgupta NP, et al. Challenges and opportunities for fast charging of solid-state lithium metal batteries. ACS Energy Letters. 2021;6:3734-49.
[12] Wu J-F, Pang WK, Peterson VK, Wei L, Guo X. Garnet-type fast Li-ion conductors with high ionic conductivities for all-solid-state batteries. ACS applied materials & interfaces. 2017;9:12461-8.
[13] Hayashi A, Noi K, Tanibata N, Nagao M, Tatsumisago M. High sodium ion conductivity of glass–ceramic electrolytes with cubic Na3PS4. Journal of Power Sources. 2014;258:420-3.
[14] Kato Y, Hori S, Saito T, Suzuki K, Hirayama M, Mitsui A, et al. High-power all-solid-state batteries using sulfide superionic conductors. Nature Energy. 2016;1:1-7.
[15] Kamaya N, Homma K, Yamakawa Y, Hirayama M, Kanno R, Yonemura M, et al. A lithium superionic conductor. Nature materials. 2011;10:682-6.
[16] Seino Y, Ota T, Takada K, Hayashi A, Tatsumisago M. A sulphide lithium super ion conductor is superior to liquid ion conductors for use in rechargeable batteries. Energy & Environmental Science. 2014;7:627-31.

[17] Lee Y-G, Fujiki S, Jung C, Suzuki N, Yashiro N, Omoda R, et al. High-energy long-cycling all-solid-state lithium metal batteries enabled by silver–carbon composite anodes. Nature Energy. 2020;5:299-308.
[18] Kazyak E, Garcia-Mendez R, LePage WS, Sharafi A, Davis AL, Sanchez AJ, et al. Li penetration in ceramic solid electrolytes: operando microscopy analysis of morphology, propagation, and reversibility. Matter. 2020;2:1025-48.
[19] Cheng EJ, Sharafi A, Sakamoto J. Intergranular Li metal propagation through polycrystalline Li6. 25Al0. 25La3Zr2O12 ceramic electrolyte. Electrochimica Acta. 2017;223:85-91.
[20] Krauskopf T, Hartmann H, Zeier WG, Janek Jr. Toward a fundamental understanding of the lithium metal anode in solid-state batteries—an electrochemo-mechanical study on the garnet-type solid electrolyte Li6. 25Al0. 25La3Zr2O12. ACS applied materials & interfaces. 2019;11:14463-77.
[21] Kasemchainan J, Zekoll S, Jolly DS, Ning Z, Hartley GO, Marrow J, et al. Critical stripping current leads to dendrite formation on plating in lithium anode solid electrolyte cells. Nature materials. 2019;18:1105-11.
[22] Lewis JA, Cortes FJQ, Liu Y, Miers JC, Verma A, Vishnugopi BS, et al. Linking void and interphase evolution to electrochemistry in solid-state batteries using operando X-ray tomography. Nature Materials. 2021;20:503-10.
[23] Mistry A, Mukherjee PP. Molar volume mismatch: A malefactor for irregular metallic electrodeposition with solid electrolytes. Journal of the Electrochemical Society. 2020;167:082510.
[24] Verma A, Kawakami H, Wada H, Hirowatari A, Ikeda N, Mizuno Y, et al. Microstructure and pressure-driven electrodeposition stability in solid-state batteries. Cell Reports Physical Science. 2021;2:100301.
[25] Vishnugopi BS, Dixit MB, Hao F, Shyam B, Cook JB, Hatzell KB, et al. Mesoscale interrogation reveals mechanistic origins of lithium filaments along grain boundaries in inorganic solid electrolytes. Advanced Energy Materials. 2022;12:2102825.
[26] Lu Z, Yang Z, Li C, Wang K, Han J, Tong P, et al. Modulating Nanoinhomogeneity at Electrode–Solid Electrolyte Interfaces for Dendrite-Proof Solid-State Batteries and Long-Life Memristors. Advanced Energy Materials. 2021;11:2003811.
[27] Bielefeld A, Weber DA, Janek Jr. Microstructural modeling of composite cathodes for all-solid-state batteries. The Journal of Physical Chemistry C. 2018;123:1626-34.
[28] Bielefeld A, Weber DA, Janek Jr. Modeling effective ionic conductivity and binder influence in composite cathodes for all-solid-state batteries. ACS applied materials & interfaces. 2020;12:12821-33.
[29] Dixit MB, Parejiya A, Muralidharan N, Essehli R, Amin R, Belharouak I. Understanding implications of cathode architecture on energy density of solid-state batteries. Energy Storage Materials. 2021;40:239-49.
[30] Naik KG, Vishnugopi BS, Mukherjee PP. Kinetics or Transport: Whither Goes the Solid-State Battery Cathode? ACS Applied Materials & Interfaces. 2022.
[31] Oh DY, Nam YJ, Park KH, Jung SH, Kim KT, Ha AR, et al. Slurry-fabricable Li+-conductive polymeric binders for practical all-solid-state lithium-ion batteries enabled by solvate ionic liquids. Advanced Energy Materials. 2019;9:1802927.
[32] Riphaus N, Strobl P, Stiaszny B, Zinkevich T, Yavuz M, Schnell J, et al. Slurry-based processing of solid electrolytes: a comparative binder study. Journal of The Electrochemical Society. 2018;165:A3993.
[33] Culver SP, Koerver R, Zeier WG, Janek J. On the Functionality of Coatings for Cathode Active Materials in Thiophosphate-Based All-Solid-State Batteries. Advanced Energy Materials. 2019;9:1900626.
[34] Li X, Ren Z, Norouzi Banis M, Deng S, Zhao Y, Sun Q, et al. Unravelling the chemistry and microstructure evolution of a cathodic interface in sulfide-based all-solid-state Li-ion batteries. ACS Energy Letters. 2019;4:2480-8.
[35] Hao F, Mukherjee PP. Mesoscale analysis of the electrolyte-electrode interface in all-solid-state Li-ion batteries. Journal of The Electrochemical Society. 2018;165:A1857.

[36] Wan H, Mwizerwa JP, Qi X, Xu X, Li H, Zhang Q, et al. Nanoscaled Na3PS4 solid electrolyte for all-solid-state FeS2/Na batteries with ultrahigh initial coulombic efficiency of 95% and excellent cyclic performances. ACS applied materials & interfaces. 2018;10:12300-4.
[37] Koerver R, Zhang W, de Biasi L, Schweidler S, Kondrakov AO, Kolling S, et al. Chemo-mechanical expansion of lithium electrode materials–on the route to mechanically optimized all-solid-state batteries. Energy & Environmental Science. 2018;11:2142-58.
[38] Koerver R, Aygün I, Leichtweiß T, Dietrich C, Zhang W, Binder JO, et al. Capacity fade in solid-state batteries: interphase formation and chemomechanical processes in nickel-rich layered oxide cathodes and lithium thiophosphate solid electrolytes. Chemistry of Materials. 2017;29:5574-82.
[39] Zhang W, Schröder D, Arlt T, Manke I, Koerver R, Pinedo R, et al. (Electro) chemical expansion during cycling: monitoring the pressure changes in operating solid-state lithium batteries. Journal of Materials Chemistry A. 2017;5:9929-36.
[40] Davis AL, Goel V, Liao DW, Main MN, Kazyak E, Lee J, et al. Rate Limitations in Composite Solid-State Battery Electrodes: Revealing Heterogeneity with Operando Microscopy. ACS Energy Letters. 2021;6:2993-3003.
[41] Otoyama M, Kowada H, Sakuda A, Tatsumisago M, Hayashi A. Operando confocal microscopy for dynamic changes of Li+ ion conduction path in graphite electrode layers of all-solid-state batteries. The journal of physical chemistry letters. 2020;11:900-4.
[42] Otoyama M, Sakuda A, Hayashi A, Tatsumisago M. Optical microscopic observation of graphite composite negative electrodes in all-solid-state lithium batteries. Solid State Ionics. 2018;323:123-9.
[43] Neumann A, Randau S, Becker-Steinberger K, Danner T, Hein S, Ning Z, et al. Analysis of interfacial effects in all-solid-state batteries with thiophosphate solid electrolytes. ACS applied materials & interfaces. 2020;12:9277-91.
[44] Nam YJ, Oh DY, Jung SH, Jung YS. Toward practical all-solid-state lithium-ion batteries with high energy density and safety: comparative study for electrodes fabricated by dry-and slurry-mixing processes. Journal of Power Sources. 2018;375:93-101.
[45] Zhang W, Weber DA, Weigand H, Arlt T, Manke I, Schröder D, et al. Interfacial processes and influence of composite cathode microstructure controlling the performance of all-solid-state lithium batteries. ACS applied materials & interfaces. 2017;9:17835-45.
[46] Banerjee A, Park KH, Heo JW, Nam YJ, Moon CK, Oh SM, et al. Na3SbS4: a solution processable sodium superionic conductor for all-solid-state sodium-ion batteries. Angewandte Chemie. 2016;128:9786-90.
[47] Yao X, Liu D, Wang C, Long P, Peng G, Hu Y-S, et al. High-energy all-solid-state lithium batteries with ultralong cycle life. Nano letters. 2016;16:7148-54.
[48] Shi T, Tu Q, Tian Y, Xiao Y, Miara LJ, Kononova O, et al. High active material loading in all-solid-state battery electrode via particle size optimization. Advanced Energy Materials. 2020;10:1902881.
[49] Strauss F, Bartsch T, de Biasi L, Kim A-Y, Janek Jr, Hartmann P, et al. Impact of cathode material particle size on the capacity of bulk-type all-solid-state batteries. ACS Energy Letters. 2018;3:992-6.
[50] Minnmann P, Quillman L, Burkhardt S, Richter FH, Janek J. Editors' Choice—Quantifying the Impact of Charge Transport Bottlenecks in Composite Cathodes of All-Solid-State Batteries. Journal of The Electrochemical Society. 2021;168:040537.
[51] Li M, Liu T, Shi Z, Xue W, Hu Ys, Li H, et al. Dense All-Electrochem-Active Electrodes for All-Solid-State Lithium Batteries. Advanced Materials. 2021:2008723.
[52] Randau S, Walther F, Neumann A, Schneider Y, Negi RS, Mogwitz B, et al. On the Additive Microstructure in Composite Cathodes and Alumina-Coated Carbon Microwires for Improved All-Solid-State Batteries. Chemistry of Materials. 2021;33:1380-93.
[53] Müller S, Eller J, Ebner M, Burns C, Dahn J, Wood V. Quantifying inhomogeneity of lithium ion battery electrodes and its influence on electrochemical performance. Journal of The Electrochemical Society. 2018;165:A339.

[54] Kehrwald D, Shearing PR, Brandon NP, Sinha PK, Harris SJ. Local tortuosity inhomogeneities in a lithium battery composite electrode. Journal of The Electrochemical Society. 2011;158:A1393.
[55] Harris SJ, Lu P. Effects of Inhomogeneities□ Nanoscale to Mesoscale□ on the Durability of Li-Ion Batteries. The Journal of Physical Chemistry C. 2013;117:6481-92.
[56] Mistry A, Usseglio-Viretta FL, Colclasure A, Smith K, Mukherjee PP. Fingerprinting redox heterogeneity in electrodes during extreme fast charging. Journal of The Electrochemical Society. 2020;167:090542.
[57] Mistry A, Smith K, Mukherjee PP. Stochasticity at scales leads to lithium intercalation cascade. ACS applied materials & interfaces. 2020;12:16359-66.
[58] Vishnugopi BS, Verma A, Mukherjee PP. Fast charging of lithium-ion batteries via electrode engineering. Journal of The Electrochemical Society. 2020;167:090508.
[59] Chen C-F, Verma A, Mukherjee PP. Probing the role of electrode microstructure in the lithium-ion battery thermal behavior. Journal of The Electrochemical Society. 2017;164:E3146.
[60] Forouzan MM, Mazzeo BA, Wheeler DR. Modeling the effects of electrode microstructural heterogeneities on Li-ion battery performance and lifetime. Journal of The Electrochemical Society. 2018;165:A2127.
[61] Lyu P, Huo Y, Qu Z, Rao Z. Investigation on the thermal behavior of Ni-rich NMC lithium ion battery for energy storage. Applied Thermal Engineering. 2020;166:114749.
[62] Stöffler H, Zinkevich T, Yavuz M, Senyshyn A, Kulisch Jr, Hartmann P, et al. Li+-ion dynamics in β-Li3PS4 observed by NMR: Local hopping and long-range transport. The Journal of Physical Chemistry C. 2018;122:15954-65.
[63] Choi S-J, Choi S-H, Bui AD, Lee Y-J, Lee S-M, Shin H-C, et al. LiI-doped sulfide solid electrolyte: enabling a high-capacity slurry-cast electrode by low-temperature post-sintering for practical all-solid-state lithium batteries. ACS applied materials & interfaces. 2018;10:31404-12.
[64] Luo Y, Bai Y, Mistry A, Zhang Y, Zhao D, Sarkar S, et al. Effect of crystallite geometries on electrochemical performance of porous intercalation electrodes by multiscale operando investigation. Nature Materials. 2022;21:217-27.
[65] Lu X, Daemi SR, Bertei A, Kok MD, O'Regan KB, Rasha L, et al. Microstructural evolution of battery electrodes during calendering. Joule. 2020;4:2746-68.
[66] Homma K, Yonemura M, Kobayashi T, Nagao M, Hirayama M, Kanno R. Crystal structure and phase transitions of the lithium ionic conductor Li3PS4. Solid State Ionics. 2011;182:53-8.
[67] Liu Z, Fu W, Payzant EA, Yu X, Wu Z, Dudney NJ, et al. Anomalous high ionic conductivity of nanoporous β-Li3PS4. Journal of the American Chemical Society. 2013;135:975-8.

Table of Content Graphic

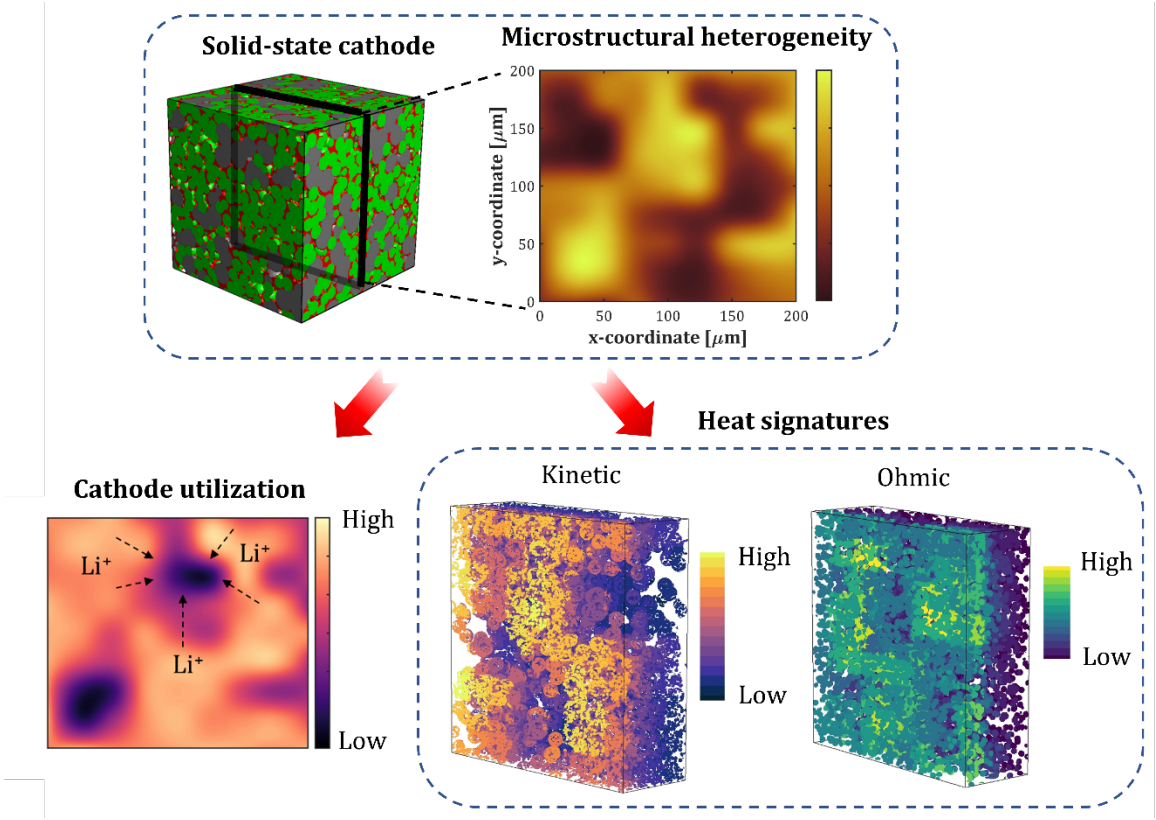

Supporting Information

Heterogeneities Affect Solid-State Battery Cathode Dynamics

Kaustubh G. Naik, Bairav S. Vishnugopi, and Partha P. Mukherjee*

School of Mechanical Engineering, Purdue University, West Lafayette, IN 47907, United States

*Correspondence: pmukherjee@purdue.edu

S1. Capturing local heterogeneities in the composite cathode microstructure

To study the role of intrinsic heterogeneities in the composite cathode of solid-state batteries (SSBs), quantifying the local electrode properties is important. Figure S1 shows a 3D schematic of a composite cathode microstructure consisting of active material (AM), solid electrolyte (SE), carbon-binder domain (CBD) and voids. To obtain the local electrode properties, cathode microstructure is divided into 9×9 representative volume elements (RVEs) and the microstructural information of each RVE is extracted (see Figure S1) and fed into the property estimation model. RVE size is taken in such a way that it is more than 3 times the size of the largest particle in the cathode microstructure (AM particle is the largest with diameter 7μm). This treatment allows us to estimate the local electrode properties, thereby capturing the electrode-scale heterogeneities, but at the same time ensure that the dimensions of RVEs are much higher than the particle sizes in the cathode microstructure. Two RVEs are shown in Figure S1 (right side), where the top RVE has sufficient SE phase which results in lower tortuosities. On the other hand, the bottom RVE has very high AM fraction, as a consequence, higher tortuosity for the ionic transport. Mathematical formulation for estimating local electrode properties is given in the subsequent section.

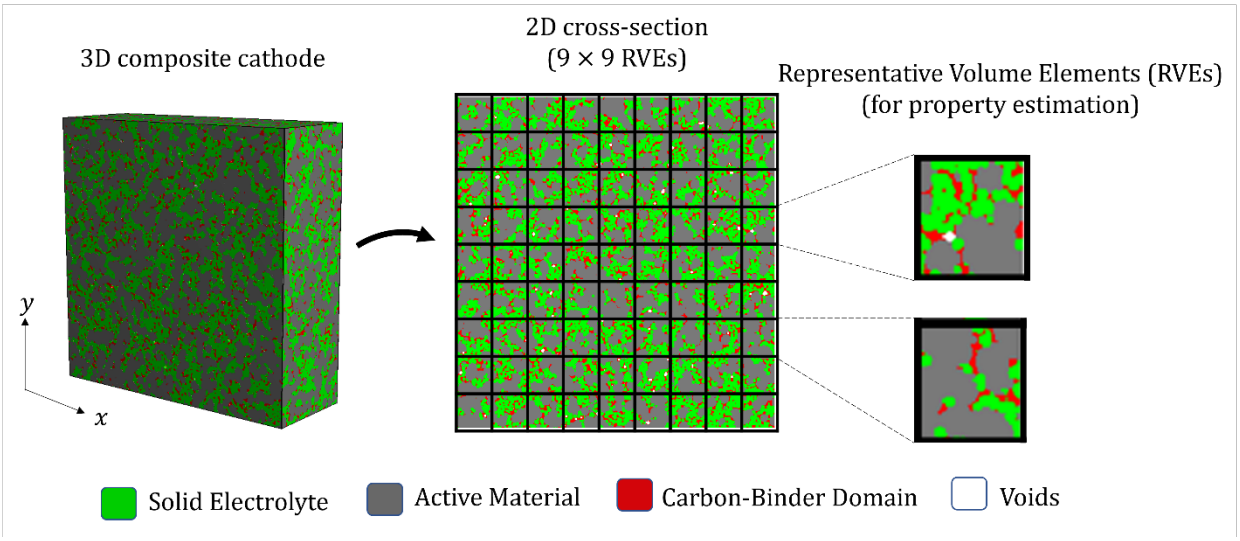

Figure S1. 3D schematic of a composite cathode microstructure followed by its 2D cross-section. Composite cathode is divided into 9 × 9 RVEs in order to extract local electrode properties such as AM loading, SE fraction, ionic tortuosity, and electrochemical active area.

S2. Mathematical formulation for estimating local electrode properties

For a solid-state composite cathode, the constituent phases comprise of active material (AM), carbon-binder domain (CBD), solid electrolyte (SE) and voids. Cathode microstructure consisting of 60 wt. % AM (NMC622), 34 wt. % SE (β-Li_3PS_4) and 6 wt. % CBD (PVDF/C) is constructed using GeoDict[1, 2]. The cathode microstructure generated is then divided into 9 × 9 Representative Volume Elements (RVEs) in xy-plane as discussed in the previous section, and the effective properties like tortuosity, ionic conductivity and electronic conductivity are estimated using the microstructural information of each RVE individually. For estimation of tortuosity, Laplace equation for electric potential needs to be solved which is given as follows:

$$\nabla^2 \phi = 0 \tag{1}$$

To estimate the *x*-direction tortuosity, τ_x, boundary conditions $\phi(x=0)=\phi_{left}$ and $\phi(x=L_x)=\phi_{right}$ are applied at $x=0$ and $x=L_x$ ends of the solid-state cathode. On the remaining faces ($y=0, z=0, y=L_y, z=L_z$), we set $\frac{\partial\phi}{\partial n}=0$. Solution obtained from Equation (1) can then be used to estimate flux by integrating the potential gradient over SE phase as follows:

$$J_z = -\int \frac{\partial\phi}{\partial z}\Big|_{z=0} dxdy \tag{2}$$

Using, Equation (2), the corresponding tortuosity can then be evaluated using:

$$j_x = -\frac{\varepsilon_{SE}}{\tau_x}\left[\frac{\phi_{right}-\phi_{left}}{L_x}\right] = -\frac{\varepsilon_{SE}}{\tau_x}\left(\frac{1}{L_x}\right) \tag{3}$$

where, ε_{SE} is the SE volume fraction and j_x is the flux in *x*-direction. Tortuosity in *y* and *z* directions can be calculated by suitably rearranging the boundary conditions mentioned for Equation (1). Tortuosity values estimated using Equation (3) are used to compute effective ionic conductivities in the x, y and z directions as follows:

$$\kappa_i^{eff} = \kappa\frac{\varepsilon_{SE}}{\tau_{SE,i=x,y,z}} \tag{4}$$

where, κ is the intrinsic ionic conductivity and $\tau_{SE,i}$ is the ionic tortuosity within the SE.

Estimation of effective electronic conductivity in AM-CBD phase requires similar procedure as described for effective ionic conductivity, that is, solving the Laplace equation for the electric potential in AM-CBD phase. Different transport coefficients in AM and CBD phases have been considered for the estimation of effective electronic conductivity. Due to the high intrinsic value of electronic conductivity of CBD phase, the effective conductivities are higher and thus, electron transport limitation is not observed in the present study. Relevant properties of AM, CBD and SE

phases have been tabulated in Table S1. Active area is calculated using the modified version of the Minkowski method[3, 4] which tracks the interfaces between the SE and AM. Mathematical expression for the estimation of the active area is given as follows:

$$a_s = \frac{4\pi I_{AM-SE}}{N_x N_y N_z \Delta} f \tag{5}$$

Here, I_{AM-SE} is the number of cell faces having AM and SE cell on either side, N_x, N_y, and N_z are the total number of cells in x, y, and z directions, respectively, and Δ is the voxel length (size of each cell). The parameter $f = \frac{N^2}{I_N}$ is obtained from the convergence of the surface area of a digitized sphere of radius $r = N\Delta$, represented by the surface faces, I_N, to that of the ideal sphere ($4\pi r^2$). It is noted that this formulation works for any geometry, thus allowing us to estimate the active area between AM and SE phases in the composite cathode.

S3. Mathematical formulation for the electrochemical performance

After obtaining the electrode properties, to model the electrochemical reactions at the AM-SE interfaces, Butler-Volmer kinetics is implemented as follows:

$$j = a_s i_{reaction} = a_s i_o \left(exp\left(\frac{F}{2RT}\left(\phi_{AM} - \phi_{SE} - U_{eq}\right)\right) - exp\left(\frac{-F}{2RT}\left(\phi_{AM} - \phi_{SE} - U_{eq}\right)\right)\right) \tag{6}$$

Here, F is the Faraday constant, R is the universal gas constant, T is the temperature (K), a_s is the active area, j is the reaction current density, U_{eq} is the equilibrium potential, and ϕ_{AM} and ϕ_{SE} are the electric potentials for electron and ion transport respectively. The exchange current density, i_o, can be expressed as follows:

$$i_0 = F k_r (c_e)^{0.5} \left(c_{s,max} - c_s\right)^{0.5} (c_s)^{0.5} \tag{7}$$

where, k_r is the reaction rate constant, c_e is the lithium-ion concentration in SE, c_s is the lithium ion concentration in AM particles and $c_{s,max}$ is the maximum lithium ion concentration that can be inserted into AM particles. U_{eq} is dependent on the state-of-charge ($\theta = c_s/c_{s,max}$) of the AM particles, and for NMC622 AM particles, the expression for U_{eq} is taken as follows[5]:

$$U_{eq} = 6.0826 - 6.9922\,\theta + 7.1062\,(\theta)^2 - 0.54549 * 10^{-4} * \exp(124.3\,\theta - 114.2593) - 2.5947\,(\theta)^3 \text{ [V]} \quad (8)$$

Lithium transport inside spherical AM particles has been solved using Ficksian diffusion equation in radial coordinates expressed as follows:

$$\frac{\partial c_s}{\partial t} = \frac{1}{r^2}\frac{\partial}{\partial r}\left(D_s r^2 \frac{\partial c_s}{\partial r}\right) \quad (9)$$

Effective ionic and electronic transport in the cathode microstructure is solved using charge conservation as follows:

Electron transport:

$$\nabla.(\sigma^{eff}\nabla\phi_{AM}) - j = 0 \quad (10)$$

Ion transport:

$$\nabla.(\kappa^{eff}\nabla\phi_{SE}) + j = 0 \quad (11)$$

All the necessary parameters used in the modeling are given in Table S2. In this work, as the effective electrode properties vary spatially, it reflects on all the physical quantities such as SE and AM phase potentials, lithium concentration in AM particles and electrochemical reaction which is discussed in detail in the main manuscript.

S4. Temperature-dependent kinetic and transport properties

To incorporate temperature-dependent ionic conductivity of β-Li_3PS_4 in the proposed model, the Arrhenius plot obtained by Stoffler *et al.*[6] is adopted and is recreated as shown in Figure S2. The Arrhenius equation for the ionic conductivity can be expressed as follows:

$$\kappa = \kappa_0 \exp\left[\frac{E_{a,\kappa}}{R}\left(\frac{1}{T} - \frac{1}{T_{ref}}\right)\right] \tag{12}$$

Here, κ_0 is the ionic conductivity of β-Li_3PS_4 at the reference temperature (T_{ref}). The activation energy, $E_{a,\kappa}$, obtained using the Arrhenius plot (Figure S2) is 0.36 eV (same as 34.7 kJ/mol). Electrochemical performance has been analyzed for five different temperatures in our work: -20 °C, 0 °C, 20 °C, 40 °C, and 60 °C. The corresponding ionic conductivities obtained are 0.001 S/m, 0.003 S/m, 0.0093 S/m, 0.0194 S/m, and 0.04 S/m, respectively.

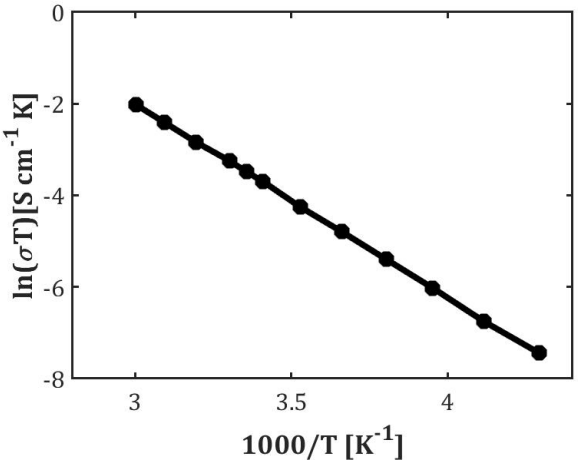

Figure S2. Arrhenius plot of ionic conductivity of β-Li_3PS_4 obtained using impedance spectroscopy by Stoffler *et al.*[6]

Temperature dependent solid-state lithium diffusivity and reaction rate constant are also incorporated based on Arrhenius equation as follows[7]:

$$D_s = D_{s_0} \exp\left[\frac{E_{a,D_s}}{R}\left(\frac{1}{T} - \frac{1}{T_{ref}}\right)\right] \tag{13}$$

$$k_r = k_{r_0} \exp\left[\frac{E_{a,k_r}}{R}\left(\frac{1}{T} - \frac{1}{T_{ref}}\right)\right] \tag{14}$$

Here, D_{s_0}, k_{r_0} are the lithium diffusivity of NMC622 and reaction rate constant at the reference temperature (T_{ref}), E_{a,D_s} and E_{a,k_r} are the corresponding activation energies. All the parameters involved in the modeling framework are given in the Table S2.

S5. Model Verification

In this section, we provide a quantitative comparison between the proposed modeling results and experimental results reported in the literature. Recently, Choi *et al.*[8], using low temperature post-sintering process for the slurry cast composite electrode showed promising performance for SSBs by minimizing the interfacial resistances within the composite electrode. Li-I doped Li_3PS_4 SE with mean particle size of 1.5 μm, NMC622 with 4 μm particle diameter, conducting additives and binder were used to design a composite solid-state cathode. Ionic conductivity of Li-I doped Li_3PS_4 SE is as high as 1×10^{-3} S cm^{-1}. Composition of the cathode used in the above-mentioned experimental study is 70 wt. % AM, 25 wt. % SE, 2.5 wt. % conducting additives and 2.5 wt. % binder, whereas the thickness is 50 μm. Using the same design parameters and 0.1 C-rate, electrochemical performance for a homogeneous electrode is obtained using the modeling framework proposed in this work. Discharge capacities (AM mass specific) obtained using the experiments and our model is compared in Figure S3. Experimental data plotted in Figure S3 is

extracted from Figure 4(b) presented in Choi *et al.*[8]. Result obtained using the computational model agrees well with the experimental data. The mismatch between the experimentally observed and computationally predicted voltage response could be due to the difference in the electrode equilibrium potentials between the two cases. Also, it is noted that the electrode properties such as tortuosity in the SE phase, electronic conductivity and active area may be different in the two cases as these properties are intricately dependent on the solid-solid contacts and connectivity within the cathode microstructure.

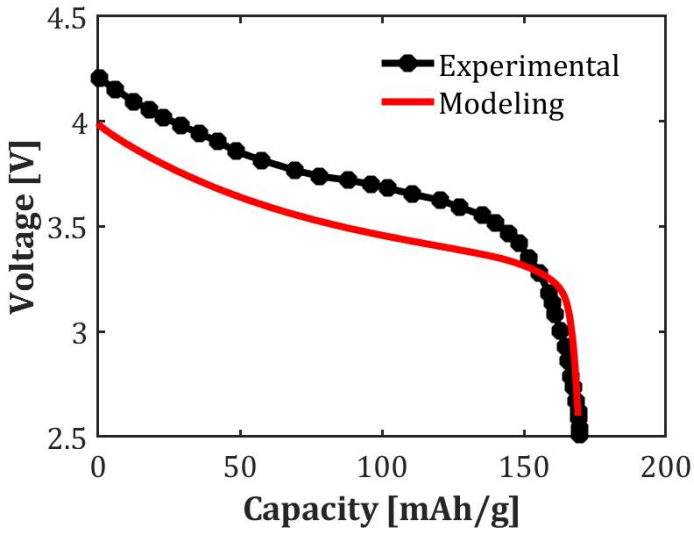

Figure S3. Comparison between modeling and experimental results showing discharge capacities for cathode compositions of 70 wt. % AM, 25 wt. % SE, 5 wt. % CBD, electrode thickness of 50 μm and discharge rate of 0.1C.

S6. Estimating Temperature rise in SSB due to the Intrinsic Heat Generation

In this section, we estimate an average temperature rise within the SSB due to internal heat generation in composite cathode. As a case study, we consider the example presented in Figure 6 of the main manuscript. Main factors responsible for the temperature rise within the battery are:

(a) heat generated within the battery, and (b) heat dissipated to the surroundings. The corresponding expression to estimate the average temperature rise can be given as follows:

$$m_{cell} C_p \Delta T = Q_{gen} - Q_{out} \quad (15)$$

Here, m_{cell} is the mass of the SSB cell, C_p is the average heat capacity, ΔT is the temperature rise, Q_{gen} is the internal heat generated, and Q_{out} is the heat dissipated to the surroundings.

It is noted that, internal heat generated within the SSB is majorly contributed by the composite cathode. Thus, here, we consider that the total heat generated within the SSB is entirely contributed by the composite cathode. To demonstrate a representative temperature rise, Q_{gen} values are taken from the results presented in Figure 6 of the main manuscript. Other parameters used for the temperature rise estimation are given in Table S3. To estimate the upper limit of temperature that the cell can reach, we consider a representative adiabatic case where the entire internal heat generation contributes to the temperature rise. Based on this, the average temperature rise of the SSB cell for the 1C discharge case presented in Figure 6 of the manuscript is 37.5 °C.

Table S1. Relevant properties for AM, SE and CBD phases considered in composite cathode microstructure[1, 2, 9].

Constituent Phase Material	**Density (g/cm^3)**	**Intrinsic electronic conductivity (S/m)**	**Intrinsic ionic conductivity (S/m)**	**Particle diameter (μm)**
NMC622 (AM)	4.7	1.06×10^{-3}	N/A	7
PVDF/C (Secondary Phase)	1.78	760	N/A	N/A
β-Li_3PS_4 (SE)	1.87	N/A	0.0093 (at 20 °C)	2

Table S2. Parameters used in the modeling framework.

Parameters		**Values**	**Units**
R	Gas constant	8.314	J mol^{-1} K^{-1}
F	Faraday constant	96,487	C mol^{-1}
N_a	Avogadro constant	6.022×10^{23}	mol^{-1}
k_b	Boltzmann constant	1.38×10^{-23}	m^2 kg s^{-2} K^{-1}
L_s	Separator thickness	100	μm
a_0	Cross-sectional area	0.0004	cm^2
$c_{s_{max}}$	Maximum lithium concentration	52500	mol m^{-3}

c_e	Lithium-ion concentration in SE	1200	mol m^{-3}
x_{in}	Initial state of charge	0.3	
D_{s_0}	Active material diffusivity	3×10^{-14}	m^2 s^{-1}
k_{r_0}	Reaction rate constant for NMC622	2.57×10^{-11}	$m^{2.5}$ $mol^{-0.5}$ s^{-1}
κ_0	Ionic conductivity of β-Li_3PS_4	0.0093	S m^{-1}
E_{a,D_s}	Activation energy for solid phase diffusivity of lithium within NMC622	20	kJ mol^{-1}
E_{a,k_r}	Activation energy for reaction rate constant	30	kJ mol^{-1}
$E_{a,\kappa}$	Activation energy for ionic conductivity	34.7	kJ mol^{-1}
T_{ref}	Reference temperature	293	K

Table S3. Parameters used to estimate average temperature rise of the SSB[10].

Parameters		**Values**	**Units**
L_a	Anode thickness	50	μm
L_{Al}	Aluminum current collector thickness	15	μm
L_{Cu}	Copper current collector thickness	10	μm
C_p	Heat capacity of the SSB	1200	J kg^{-1} K^{-1}
ρ_a	Density of Li anode	0.54	g cm^{-3}

ρ_{Al}	Density of aluminum	2.7	g cm^{-3}
ρ_{Cu}	Density of copper	8.96	g cm^{-3}
h	Convective heat transfer coefficient	0	W m^{-2} K^{-1}

References:

[1] Vishnugopi BS, Verma A, Mukherjee PP. Fast charging of lithium-ion batteries via electrode engineering. Journal of The Electrochemical Society. 2020;167:090508.
[2] Chen C-F, Verma A, Mukherjee PP. Probing the role of electrode microstructure in the lithium-ion battery thermal behavior. Journal of The Electrochemical Society. 2017;164:E3146.
[3] Parmananda M, Norris C, Roberts SA, Mukherjee PP. Probing the Role of Multi-scale Heterogeneity in Graphite Electrodes for Extreme Fast Charging. ACS Applied Materials & Interfaces. 2022;14:18335-52.
[4] Naik KG, Vishnugopi BS, Mukherjee PP. Kinetics or Transport: Whither Goes the Solid-State Battery Cathode? ACS Applied Materials & Interfaces. 2022.
[5] Barai P, Rojas T, Narayanan B, Ngo AT, Curtiss LA, Srinivasan V. Investigation of Delamination-Induced Performance Decay at the Cathode/LLZO Interface. Chemistry of Materials. 2021;33:5527-41.
[6] Stöffler H, Zinkevich T, Yavuz M, Senyshyn A, Kulisch Jr, Hartmann P, et al. Li+-ion dynamics in β-Li3PS4 observed by NMR: Local hopping and long-range transport. The Journal of Physical Chemistry C. 2018;122:15954-65.
[7] Lyu P, Huo Y, Qu Z, Rao Z. Investigation on the thermal behavior of Ni-rich NMC lithium ion battery for energy storage. Applied Thermal Engineering. 2020;166:114749.
[8] Choi S-J, Choi S-H, Bui AD, Lee Y-J, Lee S-M, Shin H-C, et al. LiI-doped sulfide solid electrolyte: enabling a high-capacity slurry-cast electrode by low-temperature post-sintering for practical all-solid-state lithium batteries. ACS applied materials & interfaces. 2018;10:31404-12.
[9] Garcia-Mendez R, Smith JG, Neuefeind JC, Siegel DJ, Sakamoto J. Correlating macro and atomic structure with elastic properties and ionic transport of glassy Li2S-P2S5 (LPS) solid electrolyte for solid-state Li metal batteries. Advanced Energy Materials. 2020;10:2000335.
[10] Chen R, Nolan AM, Lu J, Wang J, Yu X, Mo Y, et al. The thermal stability of lithium solid electrolytes with metallic lithium. Joule. 2020;4:812-21.